Defect-balanced Active and Stable Co_3O_{4-x} for Proton Exchange Membrane Water Electrolysis at Ampere-level Current Density

*Chengli Rong,[1] Shuhao Wang,[1, 2] Xin Shen,[2] Chen Jia,[1] Qian Sun,[1] Qiang Zhang,[2] Chuan Zhao[1]**

[1]School of Chemistry, The University of New South Wales Sydney, NSW 2052, Australia

*Email: chuan.zhao@unsw.edu.au

[2]Beijing Key Laboratory of Green Chemical Reaction Engineering and Technology Department of Chemical Engineering, Tsinghua University, Beijing 100084, China

Supporting information

1. Experimental Section

Materials: cobalt nitrate **(**$Co(NO_3)_2 \cdot 6H_2O$), 2-methylimidazole (2-MIM), tannic acid (TA), cetyltrimethylammonium bromide (CTAB), Nafion® (5 wt. % in a mixture of lower aliphatic alcohols and water), commercial ruthenium oxide (c-RuO_2), sulfuric acid (H_2SO_4), and potassium hydroxide (KOH) are were purchased from Sigma-Aldrich.

1.1 Synthesis of ZIF-67 nanocubes (NCs): 584 mg of $Co(NO_3)_2 \cdot 6H_2O$ and 8 mg cetyltrimethylammonium bromide was dissolved in 20 mL water, and then rapidly injected into 140 mL solution with 9.08 g of 2-methylimidazole, stirred for 30 min. The product was collected by centrifugation and then dispersed into 40 mL ethanol.

1.2 Synthesis of Co_3O_4 nanoparticles with oxygen vacancies in hollow nanocubes (V_o-Co_3O_4 HNCs): The ZIF-67 NCs solution was poured into 600 ml solution (v_{H2O}:$v_{Ethanol}$=1:1) with 600 mg TA and then stirred for 10 min. The product was collected by centrifugation, washed with ethanol, and dried at 70℃ in air. Then, the TA-Co HNCs was annealed at 600℃ for 1 h under N_2 to yield Co@C HNCs. And then, Co@C HNCs were annealed at 200℃ for 6 h in air to generate pristine Co_3O_4 HNCs (denoted as p-Co_3O_4 HNCs). Then, the p-Co_3O_4 HNCs is further reduced by 0.5 M $NaBH_4$ at 30 min (V_o-Co_3O_4 HNCs), 60 min (30% V_o-Co_3O_4 HNCs), and 120 min (39% V_o-Co_3O_4 HNCs) to get the final product.

1.3 Synthesis of bulk Co_3O_4 nanoparticles with oxygen vacancies (V_o-Co_3O_4 Bulk): ZIF-67 NCs was annealed at 600℃ for 1 h under N_2 to yield Co@C. And then, the Co@C was annealed at 200℃ for 6 h in air. Then, Co_3O_4 was further reduced by 0.5 M $NaBH_4$ for 30 min to get the final product.

2. Characterizations

2.1 Physical Characterizations: Scanning electron microscope (SEM) images were collected with a QUANTA 450. Transmission electron microscopy (TEM) images were collected on JEOL JEM-ARM200f microscope at 200 kV. XRD was performed on Philips X' Pert Pro Super

X-ray diffractometer with Cu Kα radiation. Raman spectra were collected from 100 to 3200 cm^{-1} at 532 nm. Fourier transform infrared (FTIR) spectra were collected on IRPrestige-21 from 400 to 4000 cm^{-1}. Thermogravimetric analysis (TGA) was performed on the Shimadzu DRG-60 thermal analyzer under air. Brunauer-Emmett-Teller (BET) surface areas were measured on Tristar II 3020 by nitrogen adsorption-desorption at 77 K. For NH_3-temperature program desorption (NH_3-TPD), all samples were preheated at 300 °C for 1 h with Ar to clean the surface, then NH_3 was chemisorbed at 100 °C for 1 h. The chemisorbed NH_3 was desorbed by increasing the temperature to 600 °C at 10 °C min^{-1}. XPS results were performed by Thermo ESCALAB250i and all the binding energies were calibrated by referencing C 1s to 284.5 eV. The Co K-edge X-ray absorption fine structure (XAFS) was collected at Australian Synchrotron.

3. Electrochemical tests

3.1 Preparation of the working electrode: 5.0 mg catalyst was dispersed in a mixture of 0.75 mL of water, 0.25 ml of ethanol, and 30 μl of 5% Nafion (Sigma Aldrich, 5 wt.%) and sonicated for 30 min to form a uniform ink. After that, the catalyst ink was deposited on carbon fiber paper to form a uniform thin film (loading: 1 mg cm^{-2}). All electrochemical studies were performed in a three-electrode system with Hg/Hg_2SO_4 as a reference electrode and graphite plate as a counter electrode, respectively. The Linear sweep voltammetry (LSV) curves were collected at 5 mV s^{-1} and 85% iR-compensation in O_2-saturated 0.5 M H_2SO_4 and 1 M KOH for acidic and alkaline OER, respectively. All the potentials were converted to a reversible hydrogen electrode (RHE): $E_{RHE} = E_{SCE} + 0.641\ V + 0.059 \times pH$.

3.2 Stability tests were conducted by chronopotentiometry method and electrochemical impendence spectra (EIS) were collected at the frequency of 0.01 to 100 000 Hz.

3.3 In-situ Raman: in-situ electrochemical Raman spectroscopy measurements were carried out in a homemade PTFE electrochemical cell. The spectra were acquired by a Horiba XploRA Raman spectrometer equipped with a 20× objective and 20 mW 532 nm laser. The collection was carried out at 20 s exposure time. A saturated Hg/Hg_2SO_4 electrode and graphite were used

as reference and counter electrode, respectively. The working electrodes were prepared by drop-casting the catalyst ink onto 0.25 cm^2 carbon fiber paper. The Raman spectra were collected at 1.55 V *vs* RHE, with different reaction times (10 min, 20 min, 30 min, 1, 2, 3, 5, 8, 10 h, and after the OER test).

4. Calculation methods

4.1 Electrochemical active surface area (ECSA): The ECSA was obtained from the electrochemical double-layer capacitance (C_{dl}) by measuring the CV, which is expected to be linearly proportional to the ECSA. The C_{dl} was determined by measuring the non-faradaic region with different scan rates (4, 8, 12, 16, 20, and 24 mV s^{-1}) between 1.27 to 1.37 V *vs* RHE. The ECSA of the samples is calculated from the C_{dl} according to the equation: ESCA= $\frac{C_{dl}}{C_s}$, Where C_s = 0.035 mF cm^{-2} in H_2SO_4.[1]

4.2 The calculation for Turnover frequency (TOF)

The TOF of V_o-Co_3O_4 HNCs and references were calculated based on the equation:

$TOF = \frac{n_{O_2}}{n_{Co}}$ (n_{O_2}: the number of oxygen per second, n_{Co}: the number of Co participating in the OER)

The $n_{O_2}$is calculated from the LSV curve by the equation: $n_{O_2} = \frac{i_{geo}}{z * F}$

i_{geo}: the geometric current density (mA cm^{-2}), z: the number of electrons required per oxygen molecule, F: the Faraday constant (96,484 C mol^{-1}).

In our case, the values of the total oxygen turnovers were calculated from the current density obtained in the OER polarization (at an overpotential of 400 mV, the current density is 140 mA cm^{-2} for V_o-Co_3O_4 HNCs in 0.5 M H_2SO_4): $n_{O_2} = 140 * \frac{A}{cm^2} * \frac{1}{1000} * \frac{1\ mol}{4 *\ 96484\ A\ s} =$ $3.63 * 10^{-7}$ mol cm^{-2} s^{-1}

We assume that all Co atoms in the catalysts are active for OER. The number of Co atoms number in V_o-Co_3O_4 HNCs was calculated from the mass loading (1 mg cm^{-2}) on the carbon

fiber paper. The Co content in V_o-Co_3O_4 HNCs was 73 wt. %.

The n_{Co} is calculated as: $n_{Co} = \frac{m_{cat} * Cobalt\ wt\ \%}{M_{cobalt}} = \frac{73}{100} * \frac{1\ mg}{cm^2} * \frac{1}{58.93\ mg\ mol - 1}$ $=1.239*10^{-2}$ mol cm^{-2}

M_{cobalt}: molar mass of Cobalt (58.93 g mol^{-1}), m_{cat}: catalyst loading, $Co\ wt\ \%$: Co content in the catalyst.

Proton exchange membrane (PEM) water electrolyzer test

To construct the membrane electrode assembly (MEA), V_o-Co_3O_4 HNCs and commercial RuO_2 were used as the anode catalysts, and commercial Pt/C (20 wt. %) was used as the cathode catalyst. To prepare the anode and cathode ink, catalysts were dispersed to a mixture of ethanol and distilled water with a ratio of 1:1. Then, Nafion® solution (5 wt. %) was added in to obtain an ionomer amount of 30 wt. % for an anode and 40 wt. % for a cathode. After ultrasonicated for at least 1 h, a uniform catalyst ink can be obtained. Then the obtained inks were sprayed on gas diffusion layer (2 × 2 cm^2, Fuel Cell Store). The anode and cathode catalysts loading are controlled to be 2 mg cm^{-2} and 0.5 mg cm^{-2} after loading optimization. The PEM electrolyzers were operated at 80 °C with distilled water as reactant under a flow rate of 40 mL min^{-1}. The stability of the PEM electrolyzers was evaluated by measuring chronopotentiometry at 0.5 and 1 A cm^{-2}. The anode dissolution amount was determined by ICP.

Energy efficiency calculation. The energy efficiency of the PEM electrolyzer is calculated based on the equation: Energy efficiency = $\frac{1.23\ V}{U_{cell}}$

where 1.23 V is the theoretical energy of the products, U_{cell} is the cell voltage (V) required to deliver a current density of 1 A cm^{-2}.

Energy consumption calculation. The energy consumption of a PEM electrolyser is calculated by the equation: Energy consumption = $\frac{I_{cell} * U_{cell}}{m_{H_2}} t$

where I_{cell} is the delivered current (A), t is the operation time (h), m_{H2} is the mass of hydrogen produced in a t duration, which can be calculated by Faraday's laws of electrolysis: $m_{H_2} = \frac{I_{cell} * t}{z * F} M_{H_2}$

z is the number of electrons transferred to produce one hydrogen molecule (2), M_{H2} relative molecular mass (2 g mol^{-1}).

Hydrogen production cost. The electricity cost is calculated based on the energy consumption: Cost (H_2/kg) = energy consumption × electricity bill

where energy consumption is calculated at 1 A cm^{-2}, and the electricity bill is obtained from the previous reports ($0.02/Kw h)[2].

4.2 DFT calculations

All the calculations were implemented using the VASP (Vienna Ab initio Simulation Packages) code which uses a plane wave basis set for the electronic orbitals and a projector-augmented wave method for core electrons. General gradient approximation (GGA) was used with the Perdew–Burke–Ernzerhof (PBE) functional to describe the correlation exchange energy.[3] The cut-off energy was employed as 500 eV and the *k*-point sampling of the Brillouin zone was obtained using 3 x 3 x 1 by Monkhorst–Pack scheme. All structural models were entirely relaxed at the convergence criterion of 10^{-4} eV of total energy and 0.05 eV/Å of residual forces. The Hubbard U values were considered to address the strongly correlated interaction between 3d electron of Co (3.3eV).[4] The partial density of states (PDOS) of the surface atom was calculated using an integration of 7 × 7 × 1 k points meshes.

Bulk Co_3O_4 spinel unit cell (space group of $Fd\bar{3}m$) was constructed by optimizing cubic cells containing 56 ions ($Co_{24}O_{32}$). An experimentally observed (331) surface was adopted to simulate the reactive surface, which allows the top two atomic layers to relax and all the other atoms fixed in their respective bulk positions. A surface unsaturated three-coordinated Co atom is considered as active sites for oxygen evolution reaction and water adsorption. Further, coordinated oxygen on a three-coordinated Co centre was removed to simulate the oxygen vacancy environment.

The oxygen evolution reaction in acid contains four reaction intermediates, namely, the chemisorbed OH*, O*, and OOH* intermediates, were considered:

$$H_2O + * \rightarrow HO* + H^+ + e^-$$

$$OH* \rightarrow O* + H^+ + e^-$$

$$O* + H_2O \rightarrow OOH* + H^+ + e^-$$

$$OOH* \rightarrow O_2 + H^+ + e^-$$

where * stands for active sites, the free energy change should be the same at the equilibrium potential of computation hydrogen electrode.[5] For each step, the reaction Gibbs free energy (ΔG) is defined as:

$$\Delta G = \Delta E + \Delta E_{ZPE} - T\Delta S$$

where ΔE is the binding energy of adsorbed oxygen-containing intermediates from DFT calculations, ΔE_{ZPE} is zero-point energy, and ΔS is the entropy change at 298. Here, the zero-point energies and entropies of surface adsorbates are calculated by Vaspkit code.[6] The adsorption energy of water calculated is:

$$E_{adsorption} = E_{H2O*} - E_{slab*} - E_{H2O}$$

where E_{H2O*} and E_{slab*} are the computed total energies of the surfaces/interfaces with and without adsorbed H_2O.

4.3 Finite-element simulations

COMSOL Multiphysics 5.5 is employed for the finite-element simulations. The parameters used in the model are listed below (**Table S**1). The transport of OH^- in the electrolyte is given by the Nernst−Planck equation with the mass conservation:

$$N_i = -D_i \nabla c_i - z_i c_i F \frac{D_i}{RT} \nabla \phi_l \quad (1)$$

$$\frac{\partial c_i}{\partial t} = -\nabla \cdot N_i \tag{2}$$

where D_i, c_i, and z_i are the diffusion coefficient, the concentration, and the valence of species i, respectively. F, R, T, and t denote Faraday constant, ideal gas constant, temperature, and time, respectively. The electrochemical reaction on the electrode surface is described by the Bulter–Volmer equation:

$$i_{loc} = i_0\left[exp\left(\frac{\alpha F\eta}{RT}\right) - exp\left(-\frac{\beta F\eta}{RT}\right)\right] \tag{3}$$

where i_0, α, β, η represent the exchange current density, the anodic charge transfer coefficient, the cathodic charge transfer coefficient, and overpotentials. The geometries of hollow structure and bulk are constructed according to experimental morphology.

Table S1. Parameters used in the COMSOL model.

Name	Symbol	Value	Unit
Temperature	T_0	298	K
Exchange current density of hollow structure	i_0	1.7	mA cm^{-2}
Exchange current density of bulk	i_0	0.6	mA cm^{-2}
Diffusion coefficient of OH^-	D	5×10^{-9}	m^2 s^{-1}
The electric conductivity of catalysts	σ_s	1	S m^{-1}
The ionic conductivity of electrolyte	σ_l	20	mS cm^{-1}
Charge transfer coefficient	α, β	0.5	
Equilibrium potential	E_{eq}	1.23	V

5. Supplementary figures

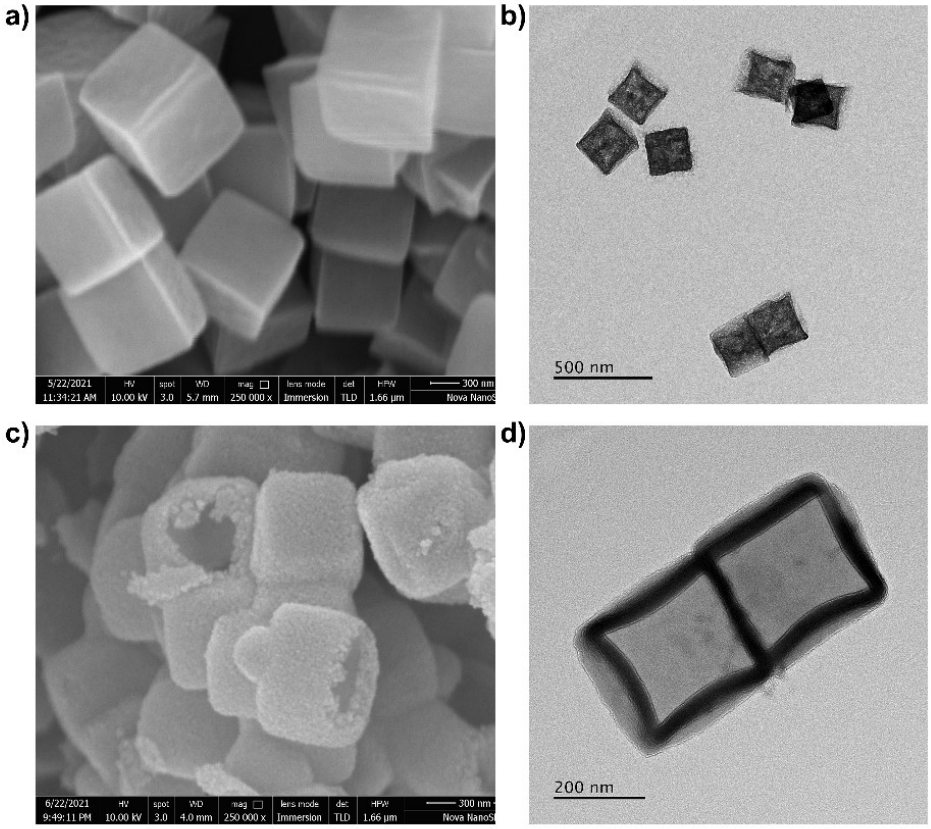

Figure S1. a) SEM and **b)** TEM images ZIF-67 NCs. **c)** SEM and **d)** TEM images TA-Co HNCs.

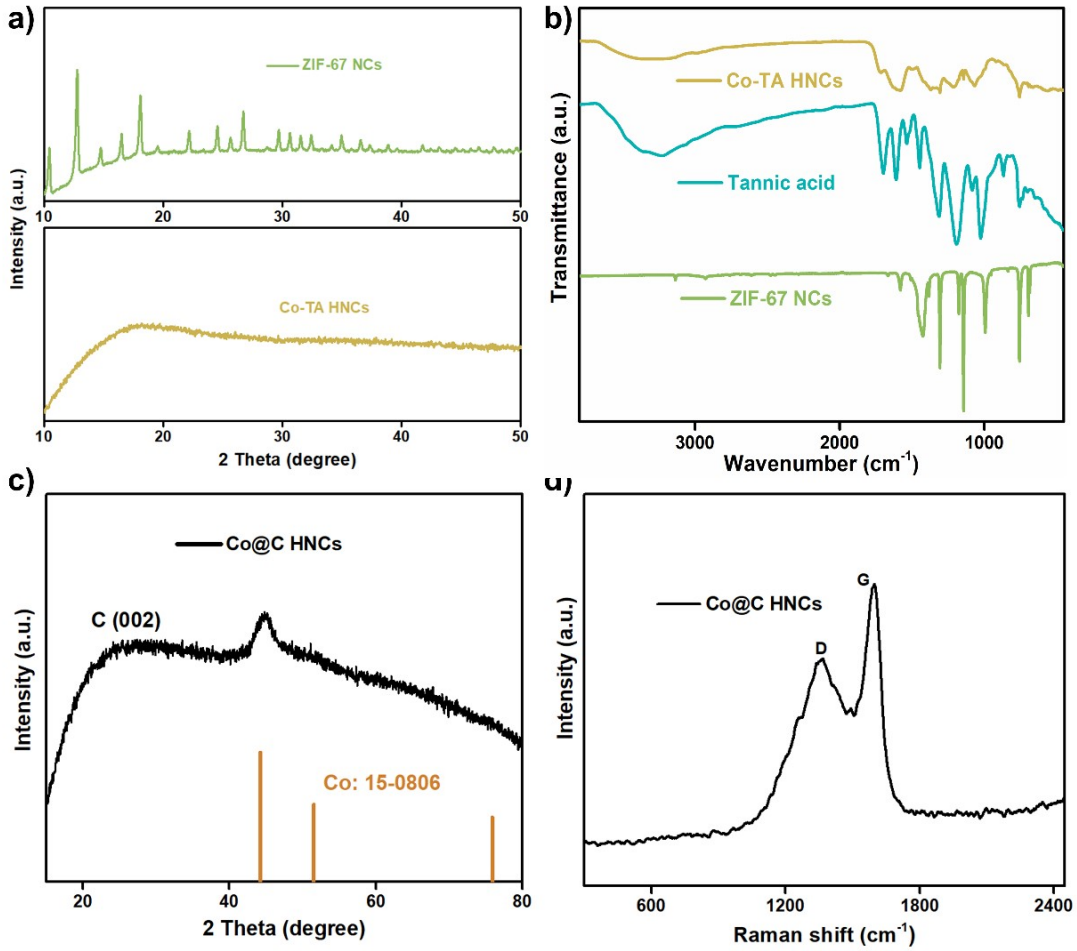

Figure S2. a) XRD patterns and **b)** FTIR spectra of ZIF-67 NCs and Co-TA HNCs. **c)** XRD patterns and **d)** Raman spectrum of ZIF-67 NCs after pyrolysis under N_2 atmosphere.

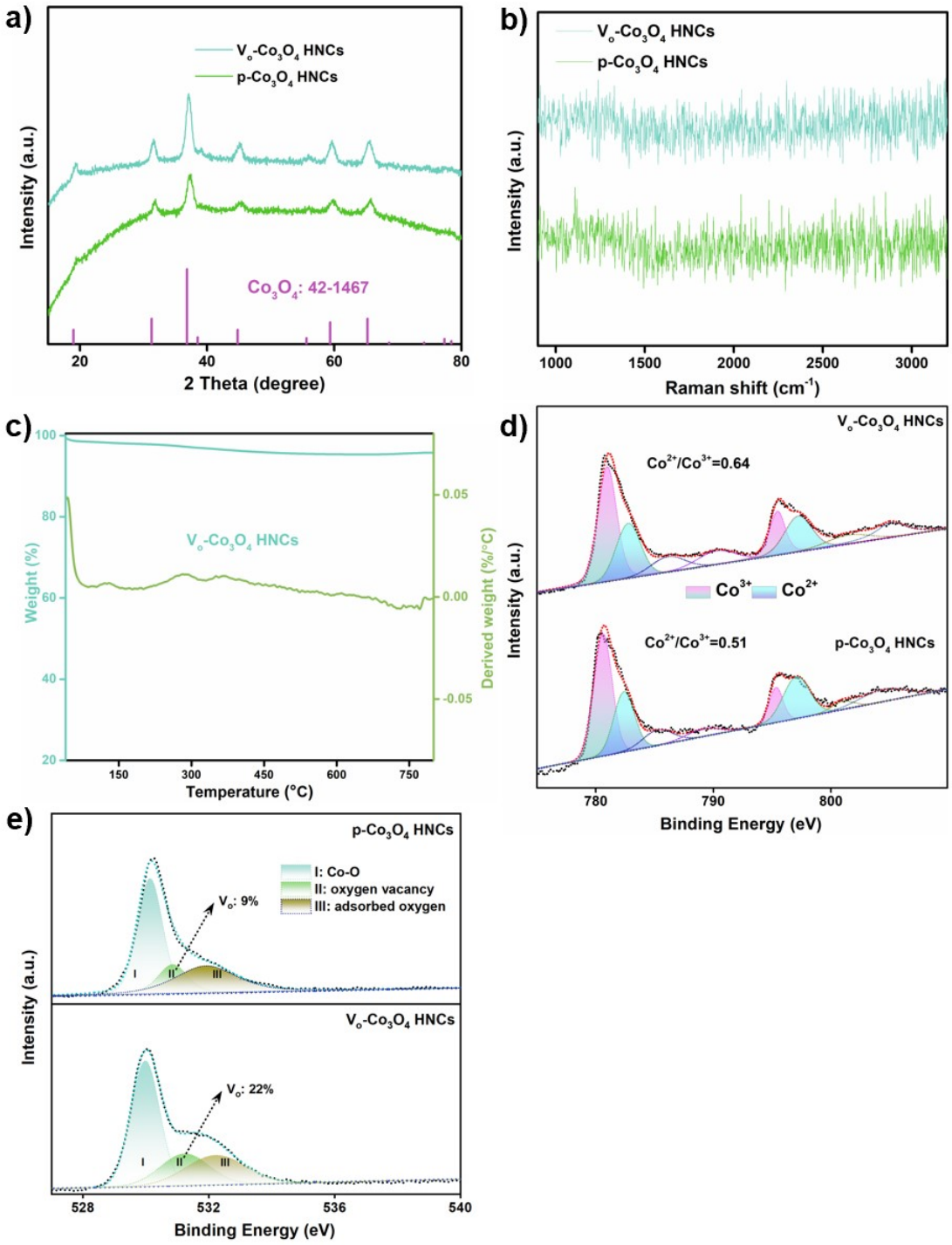

1

2 **Figure S3. a)** XRD patterns**, b)** Raman, **c)** thermogravimetric analysis, and XPS of **d)** Co 2p and **e)** O 1s

3 of V_o-Co_3O_4 HNCs and p-Co_3O_4 HNCs.

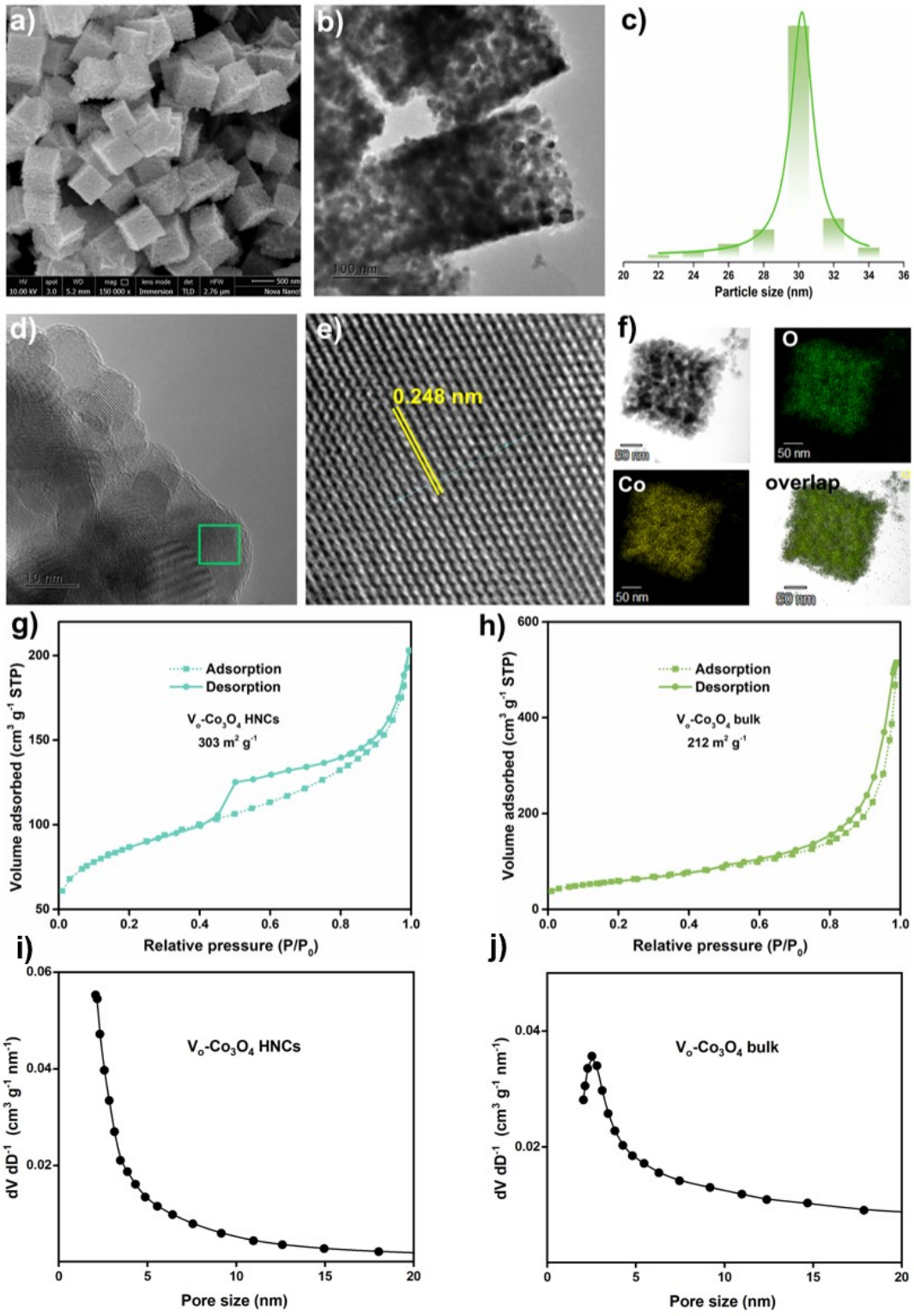

Figure S4. a) SEM, **b)** TEM, **c)** particle size distribution, **d, e)** HRTEM, and **f)** energy-dispersive X-ray spectroscopy (EDS) mapping of V_o-Co_3O_4 bulk. N_2 adsorption-desorption of **g)** V_o-Co_3O_4 HNCs and **h)** V_o-Co_3O_4 bulk. Pore size distribution of **i)** V_o-Co_3O_4 HNCs and **j)** V_o-Co_3O_4 bulk.

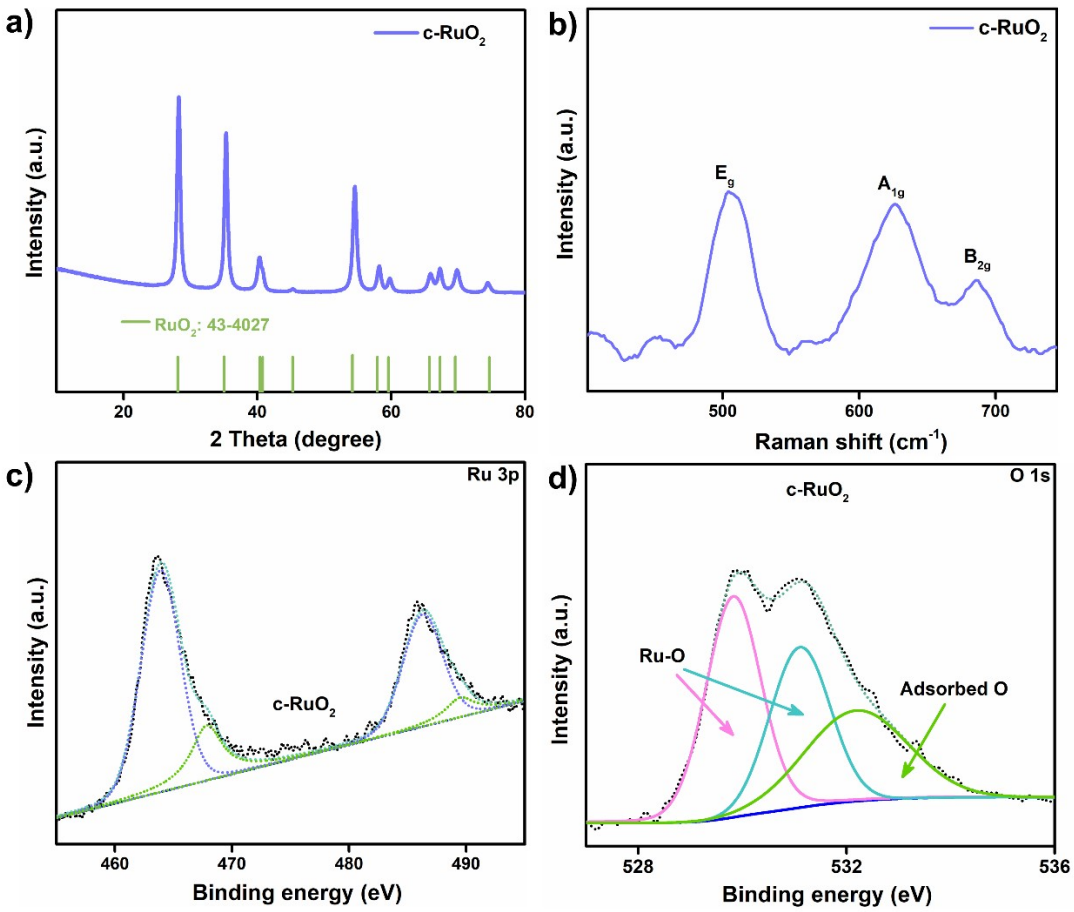

Figure S5. a) XRD pattern, **b)** Raman, XPS of **c)** Ru 3p, and **d)** O 1s of c-RuO_2.

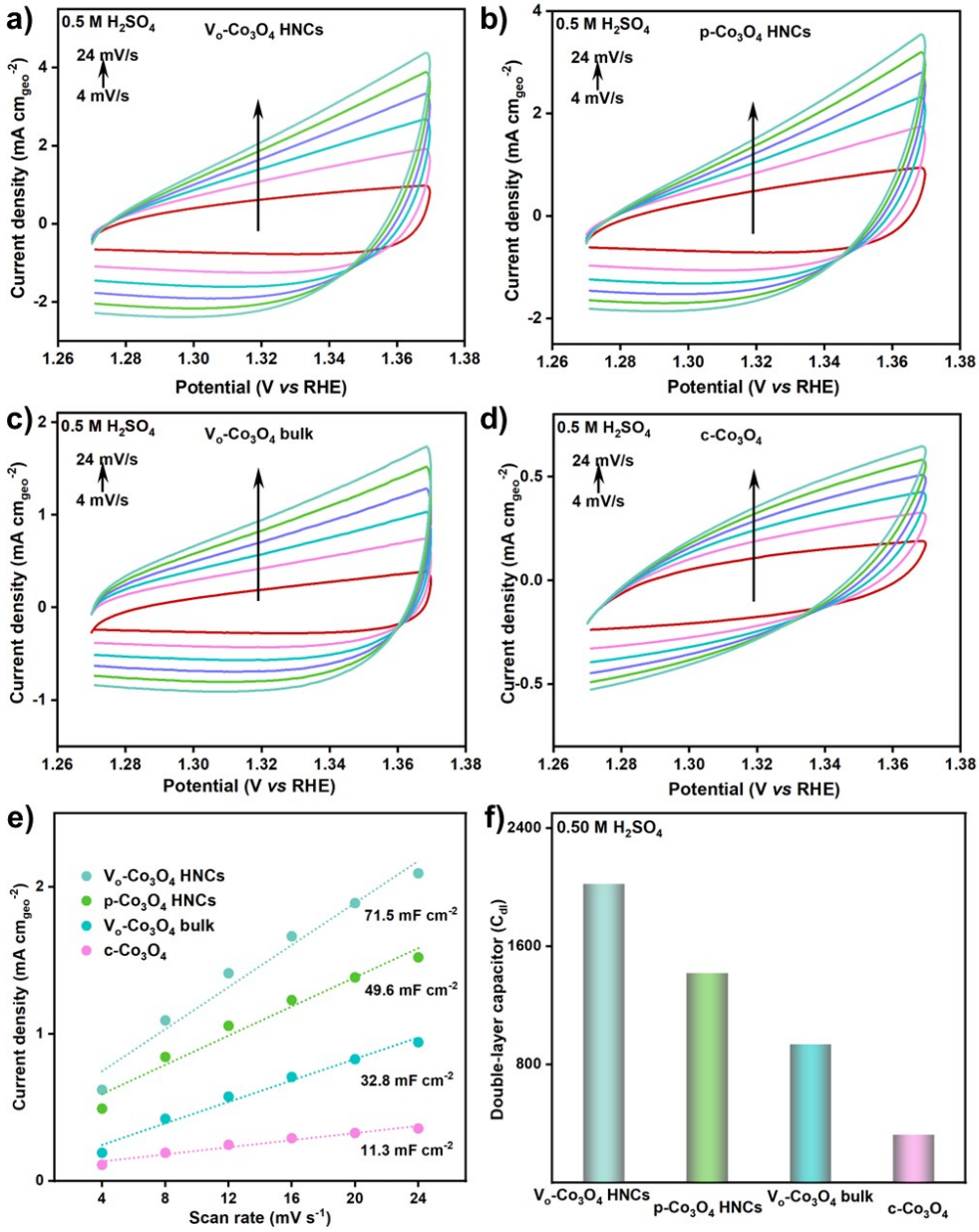

Figure S6. a-d) CV profiles of different catalysts in the non-Faradaic region of 1.27-1.37 V *vs* RHE with the scan rate of 4, 8, 12, 16, 20, 24 mV s^{-1}. **e)** The C_{dl} plots and **f)** ECSA at 1.32 V *vs* RHE as a function of scan rate in 0.5 M H_2SO_4.

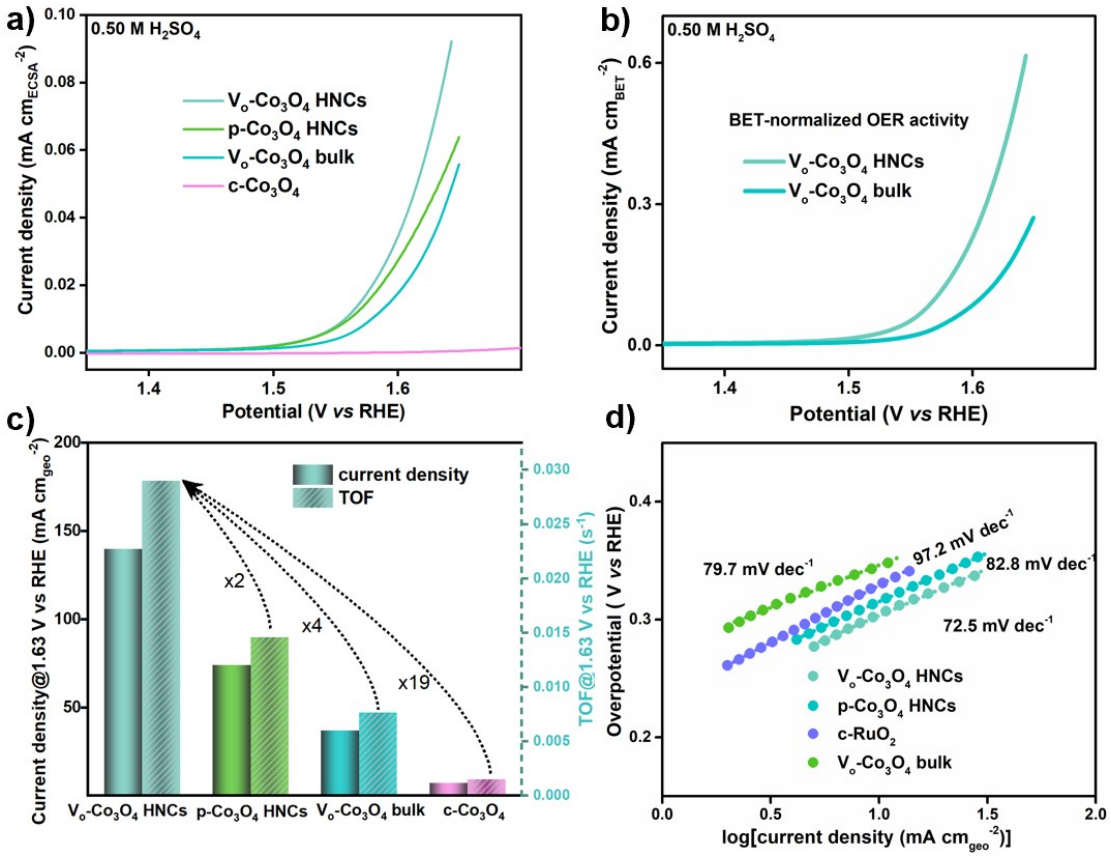

Figure S7. a) ECSA- and **b)** BET-normalized LSV curves for V_o-Co_3O_4 HNCs and reference samples in 0.5 M H_2SO_4. **c)** Comparison of the current density and TOF values at 1.63 V *vs* RHE in 0.5 M H_2SO_4. **d)** Tafel slope of V_o-Co_3O_4 HNCs, p-Co_3O_4 HNCs, c-RuO_2, and V_o-Co_3O_4 bulk in 0.5 M H_2SO_4.

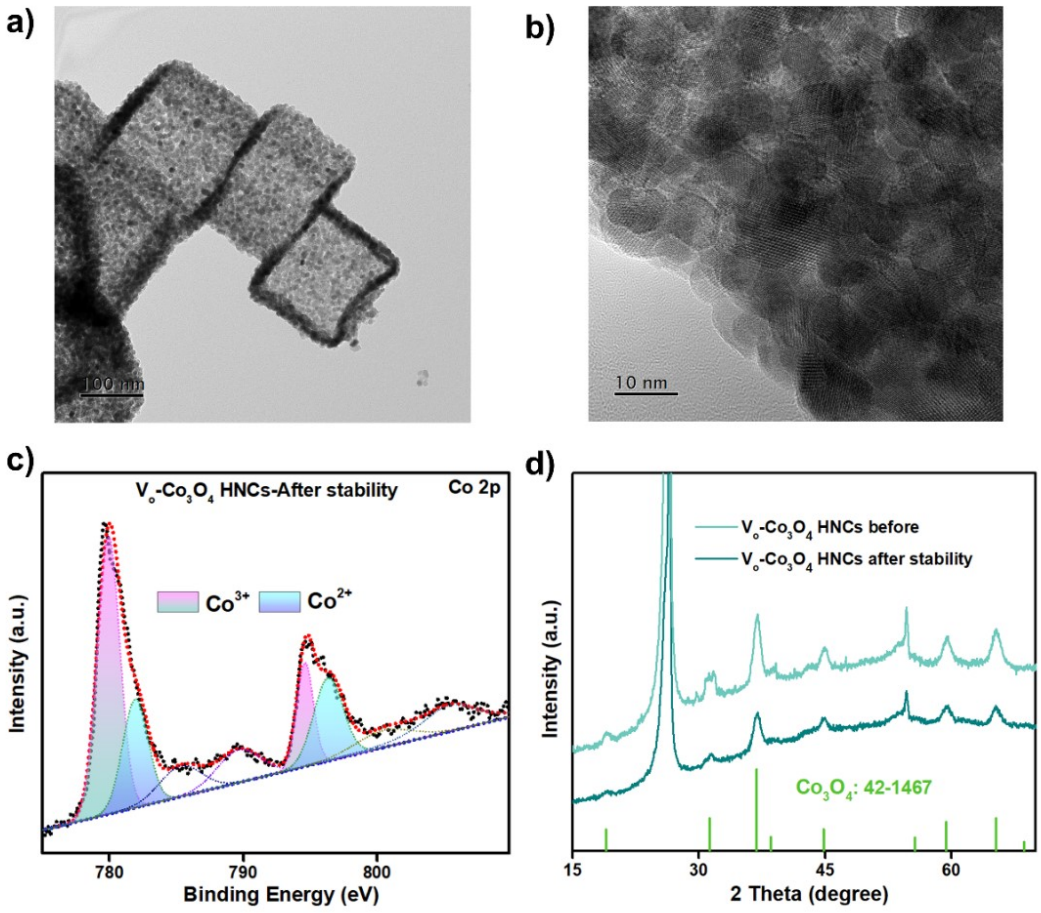

Figure S7. a, b) TEM, **c)** Co 2p XPS, and **d)** XRD for V_o-Co_3O_4 HNCs after stability test in 0.5 M H_2SO_4.

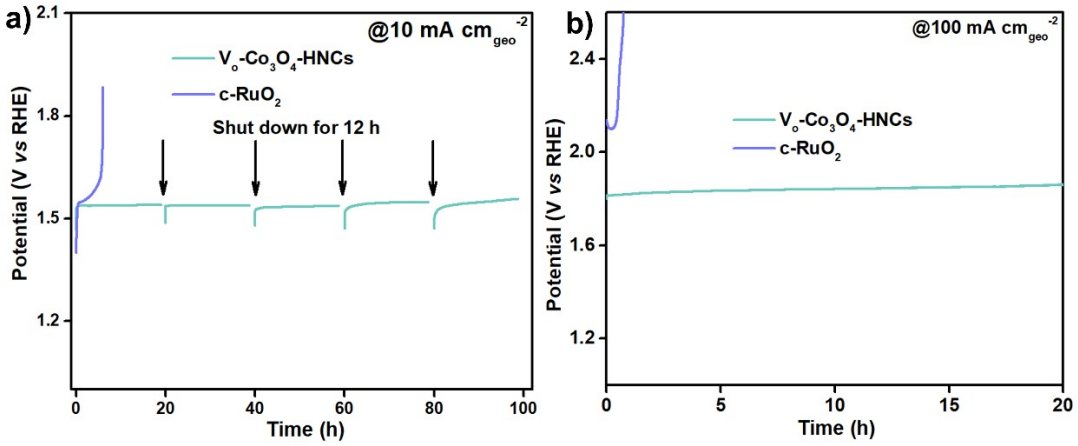

Figure S8. a) The stability test for V_o-Co_3O_4 HNCs and c-RuO_2 at 10 mA cm_{geo}^{-2} under shut on and shut down model in 0.5 M H_2SO_4. **b)** The stability test for V_o-Co_3O_4 HNCs and c-RuO_2 at 100 mA cm_{geo}^{-2} in 0.5 M H_2SO_4.

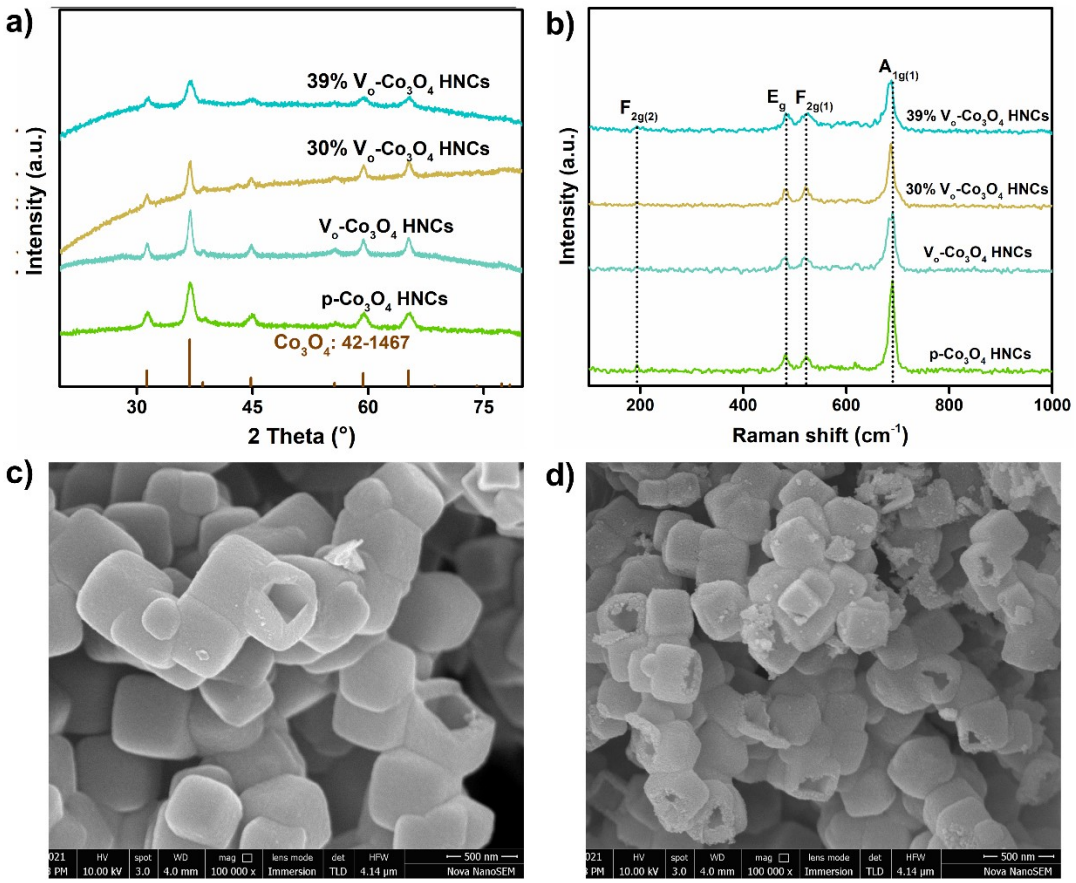

Figure S9. a) XRD patterns and **b)** Raman spectra for pristine, V_o, 30%-V_o, and 39%-V_o-Co_3O_4 HNCs.

Note: The XRD and Raman analysis suggest that the spinel structure of Co_3O_4 is still well-maintained, without generating the impure phase. This is beneficial to directly the experimental results to the concentration of oxygen vacancies.

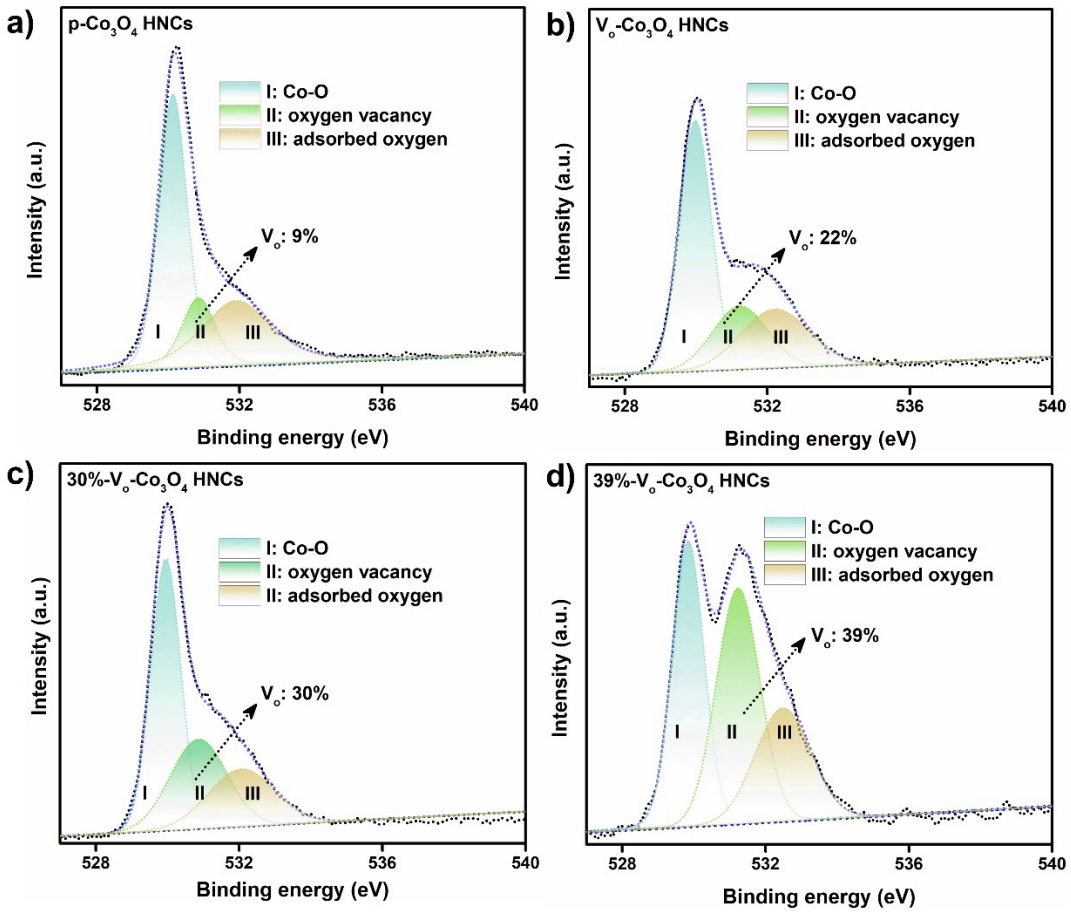

Figure S10. XPS of O 1s for **a)** pristine, **b)** V_o, **c)** 30%-V_o, and **d)** 39%-V_o-Co_3O_4 HNCs.

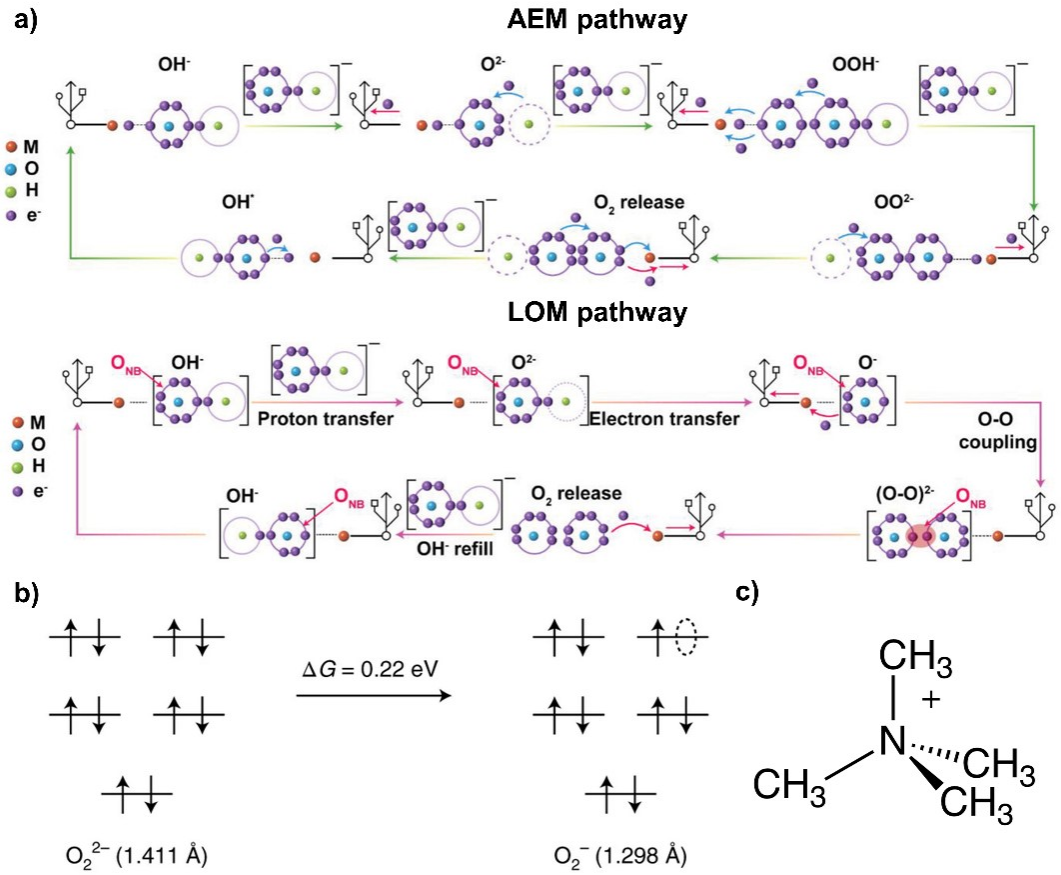

Figure S11. Electron-transfer pathways of adsorbate evolution mechanism (AEM) and lattice oxygen-evolution mechanism (LOM), respectively, reproduced from ref.[7]. b) Thermodynamic stabilities between O_2^{2-} and O_2^- species. c) tetramethylammonium cation.

Note: Recognition of peroxo-like (O_2^{2-}) and superoxo-like (O_2^-) negative species could provide indirect evidence for the proposed lattice oxygen mechanism (LOM).[7] Since the O_2^{2-} is thermodynamically more stable than O_2^-, the identification of the oxidized oxygen intermediates can offer strong evidence for corroborating the LOM mechanism.[8] Based on the previous works, tetramethylammonium cation (TMA^+) as a chemical probe is introduced to the solution because of TMA^+ cations could bind strongly to the surface of the LOM-based catalyst during OER process and inhibit the oxygen evolution by blocking these active sites. Therefore, the modulation of the OER kinetics after adding TMA^+ can be indicative of an active surface lattice oxygen.

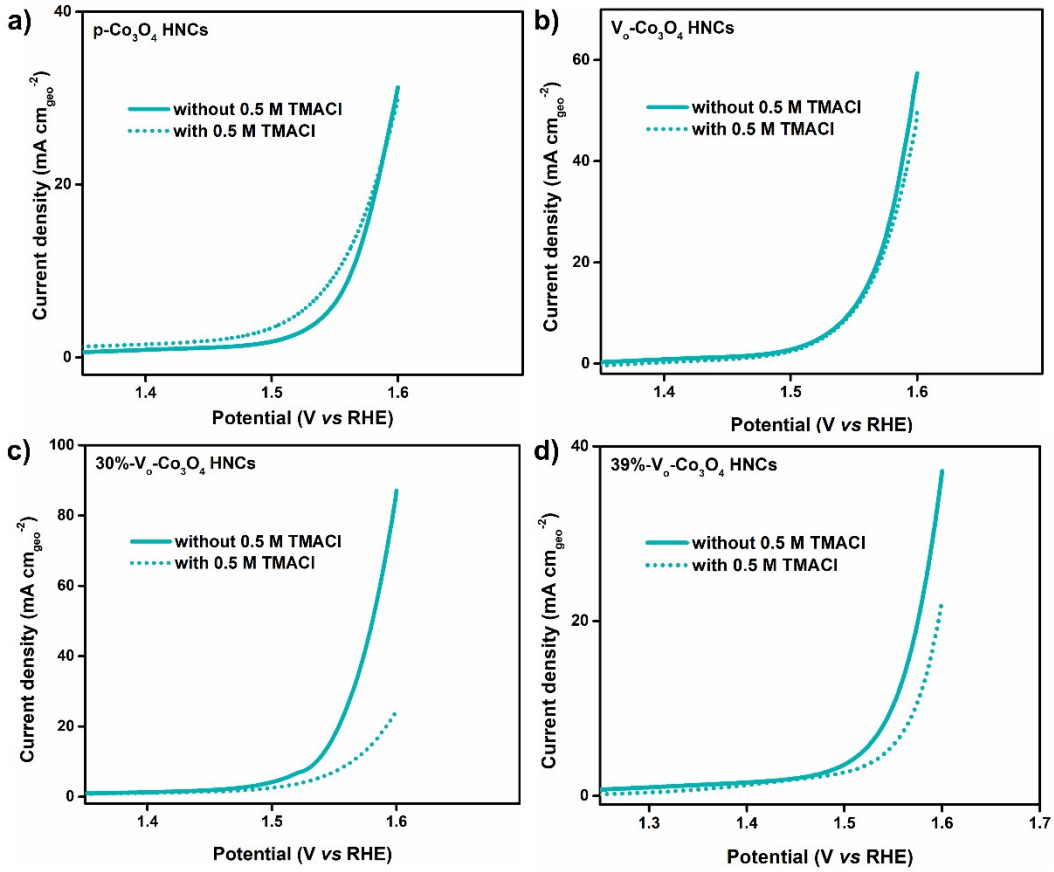

Figure S12. LSV curves of **a)** p-Co_3O_4 HNCs, **b)** V_o-Co_3O_4 HNCs, **c)** 30%-V_o-Co_3O_4, and **d)** 39%-V_o-Co_3O_4 HNCs for OER with and without adding 0.5 M TMA^+ cations in 0.5 M H_2SO_4.

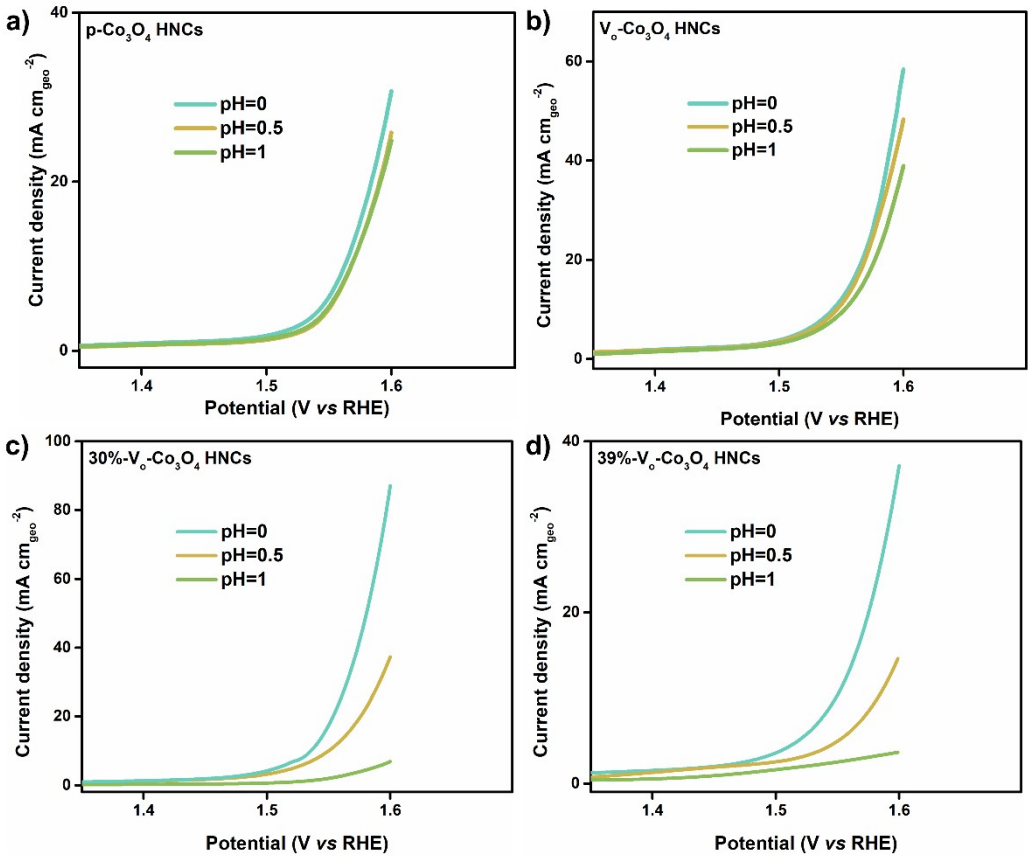

Figure S13. LSV curves of **a)** p-Co_3O_4 HNCs, **b)** V_o-Co_3O_4 HNCs, **c)** 30%-V_o-Co_3O_4, and **d)** 39%-V_o-Co_3O_4 HNCs for OER under various pH conditions. **e)** LSV curves for OER at 0.5 M H_2SO_4.

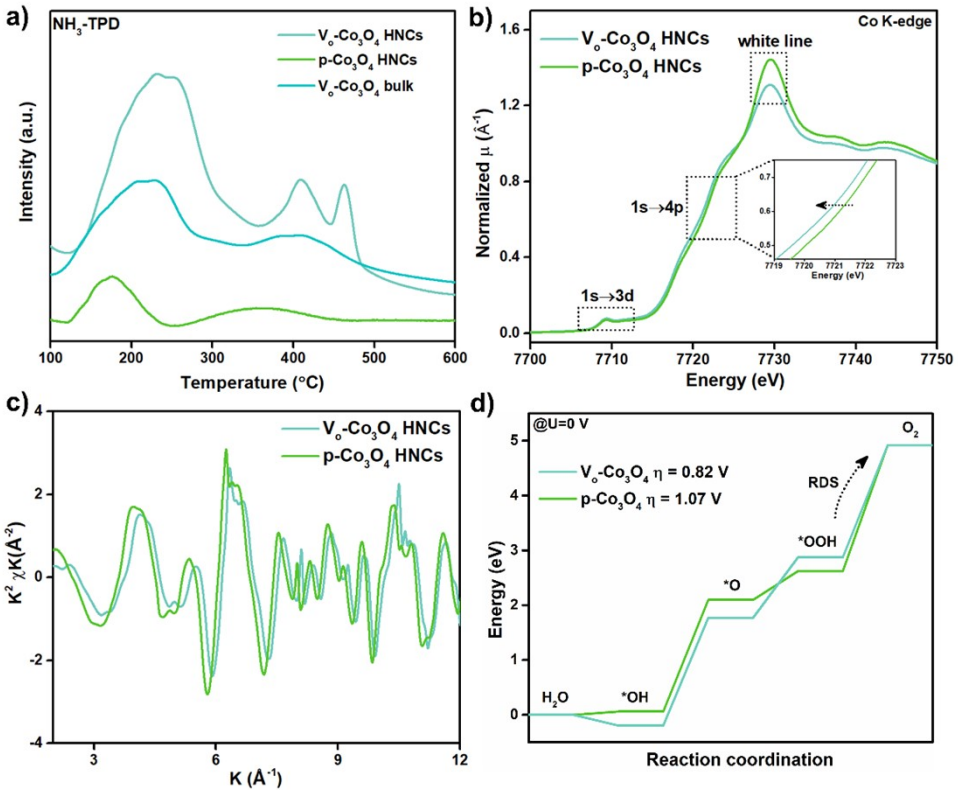

Figure S14. a) NH_3-TPD profiles of V_o-Co_3O_4 HNCs, V_o-Co_3O_4 bulk, and p-Co_3O_4 HNCs. **b)** Co K-edge XANES spectra and **c)** k^3-weight FT-EXAFS curves of V_o-Co_3O_4 HNCs and p-Co_3O_4 HNCs. **d)** Free energy diagrams for OER at pH = 0 on Co_3O_4 (311) and V_o-Co_3O_4 (311) surfaces, respectively.

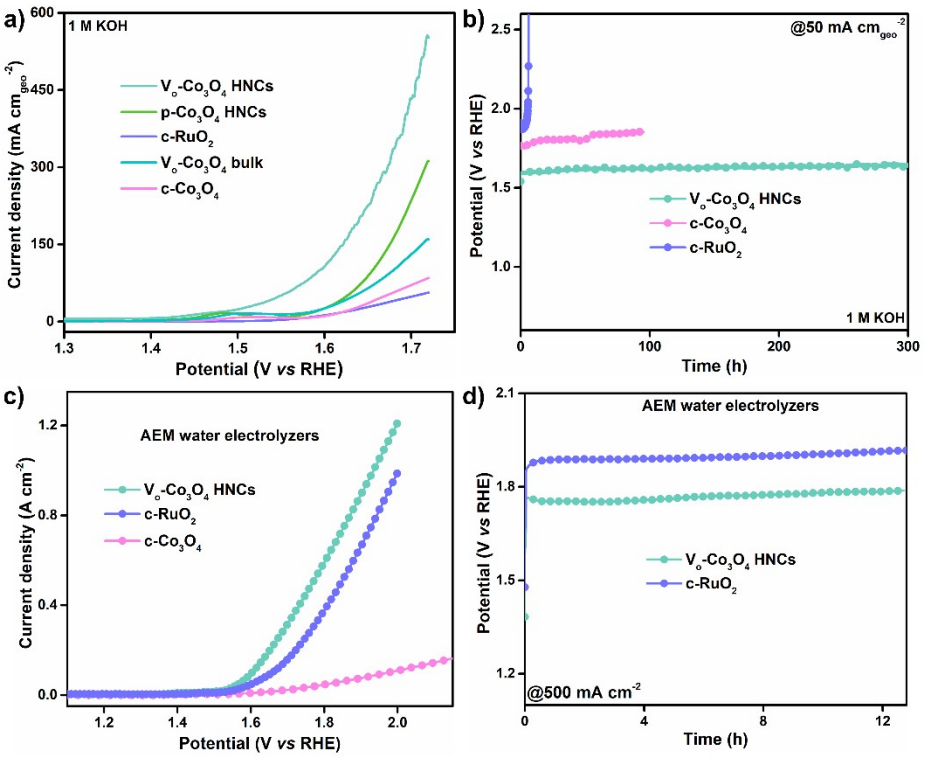

Figure S15. a) LSV and **b)** chronopotentiometry curves of V_o-Co_3O_4 HNCs and reference samples for OER in 1 M KOH. **c)** Steady-state LSV curve of anion exchange membrane electrolyser using V_o-Co_3O_4 HNCs, c-RuO_2, and c-Co_3O_4 as anode. **d)** Chronopotentiometry tests at a current density of 0.5 A cm^{-2}.

Table S2. Comparison of the reported catalysts for acidic OER.

Catalysts	Electrolyte	Mass loading mg cm^{-2}	Overpotential[a] mV	Stability	Reference
V_o-Co_3O_4 HNCs	**0.5 M H_2SO_4**	**1**	**295**	**130[b] h**	**This work**
CoSAs-MoS_2/TiN NRs	0.5 M H_2SO_4	-	454.9	45[a] h	[9]
NiFeP	0.5 M H_2SO_4	0.28	540	30[a] h	[10]
Fe_2O_3	0.5 M H_2SO_4	1	615	24[a] h	[11]
Co_3O_4/FTO	0.5 M H_2SO_4	1.8	570	12[a] h	[12]
Ru/GDY	0.5 M H_2SO_4	0.475	531	54[a] h	[13]
Ru_3Ni_3 NAs	0.5 M H_2SO_4	0.28	252	10[a] h	[14]
Ru/Co-N-C	0.5 M H_2SO_4	0.2	232	20[a] h	[15]
Ru-SA/$Ti_3C_2T_x$	0.5 M H_2SO_4	1.7	290	32[a] h	[16]
$W_{0.57}Ir_{0.43}O_{3-\sigma}$	1 M H_2SO_4	2.9	370	2000[a] s	[17]
$IrNiO_x$/Meso-ATO	0.5 M H_2SO_4	0.5	320	20[a] h	[18]
IrO_2 NN-L	0.5 M H_2SO_4	0.25	313	2[a] h	[19]
IrNi nanocluster	0.5 M H_2SO_4	0.53	350	2[a] h	[20]
Ir/Fe_4N	0.1 $HClO_4$	0.43	316	2[a] h	[21]

1T-MoS_2	0.5 M H_2SO_4	1	420	2[a] h	[22]
C60-$SWCNT_{15}$	0.5 M H_2SO_4	-	400	5[a] h	[23]
Ba[Co-POM]	1 M H_2SO_4	-	361	24[a] h	[24]
$Ir_{0.5}$W-900R	0.1 M $HClO_4$	0.13	300	100[a] h	[25]
$Ir_{0.3}Mo_{0.7}O_{\delta}$	0.1 M $HClO_4$	0.2	345	40000[a] s	[26]

Note: a, 10 mA cm_{geo}^{-2}, b, 20 mA cm_{geo}^{-2}.

Table S3. Comparison of the cell voltage at 1 A cm^{-2} in proton exchange membrane water electrolysers using V_o-Co_3O_4 HNCs as anode with reported catalysts.

	Proton exchange membrane water electrolysers			
Catalysts	Voltage/V	Energy efficiency/%	Temperature/°C	Ref.
V_o-Co_3O_4 HNCs	**1.82**	**67.6**	**60**	**This**
GB-$Ta_{0.1}Tm_{0.1}Ir_{0.8}O_{2-\delta}$	1.766	69.6	50	[2]
IrO_2 Nanoneedles	1.8	68.3	80	[27]
IrO_x/Nb-SnO_2	1.91	64.4	80	[28]
Ir/TiO_2-MoO_x	1.74	70.7	80	[29]
Ni-RuO_2	1.95	63.1	-	[30]
IrO_2-ATO	1.73	71.1	80	[31]
RuO_2@IrO_x	1.683	73.1	80	[32]
Ir@WO_x NRs	1.77	69.5	80	[33]

References

1. C. C. McCrory, S. Jung, I. M. Ferrer, S. M. Chatman, J. C. Peters and T. F. Jaramillo, *J. Am. Chem. Soc.*, 2015, **137**, 4347-4357.
2. S. Hao, H. Sheng, M. Liu, J. Huang, G. Zheng, F. Zhang, X. Liu, Z. Su, J. Hu and Y. Qian, *Nat. Nanotechnol.*, 2021, **16**, 1371-1377.
3. J. P. Perdew, K. Burke and M. Ernzerhof, *Phys. Rev. Lett.*, 1996, **77**, 3865.
4. Y. Peng, H. Hajiyani and R. Pentcheva, *ACS Catal.*, 2021, **11**, 5601-5613.
5. J. K. Nørskov, J. Rossmeisl, A. Logadottir, L. Lindqvist, J. R. Kitchin, T. Bligaard and H. Jonsson, *J. Phys. Chem. B*, 2004, **108**, 17886-17892.
6. V. Wang, N. Xu, J.-C. Liu, G. Tang and W.-T. Geng, *Comp. Phys. Commun.*, 2021, **267**, 108033.
7. X. Wang, H. Zhong, S. Xi, W. S. V. Lee and J. Xue, *Adv. Mater.*, 2022, **34**, 2107956.
8. Z.-F. Huang, J. Song, Y. Du, S. Xi, S. Dou, J. M. V. Nsanzimana, C. Wang, Z. J. Xu and X. Wang, *Nat. Energy*, 2019, **4**, 329-338.
9. T. L. L. Doan, D. C. Nguyen, S. Prabhakaran, D. H. Kim, D. T. Tran, N. H. Kim and J. H. Lee, *Adv. Funct. Mater.*, 2021, 2100233.
10. F. Hu, S. Zhu, S. Chen, Y. Li, L. Ma, T. Wu, Y. Zhang, C. Wang, C. Liu and X. Yang, *Adv. Mater.*, 2017, **29**, 1606570.
11. W. L. Kwong, C. C. Lee, A. Shchukarev, E. Björn and J. Messinger, *J. Catal.*, 2018, **365**, 29-35.
12. J. S. Mondschein, J. F. Callejas, C. G. Read, J. Y. Chen, C. F. Holder, C. K. Badding and R. E. Schaak, *chem. Mater.*, 2017, **29**, 950-957.
13. H. Yu, L. Hui, Y. Xue, Y. Liu, Y. Fang, C. Xing, C. Zhang, D. Zhang, X. Chen, Y. Du, Z. Wang, Y. Gao, B. Huang and Y. Li, *Nano Energy*, 2020.
14. J. Yang, Q. Shao, B. Huang, M. Sun and X. Huang, *iScience*, 2019, **11**, 492-504.
15. C. Rong, X. Shen, Y. Wang, L. Thomsen, T. Zhao, Y. Li, X. Lu, R. Amal and C. Zhao, *Adv. Mater.*, 2022, 2110103.
16. X. Peng, S. Zhao, Y. Mi, L. Han, X. Liu, D. Qi, J. Sun, Y. Liu, H. Bao and L. Zhuo, *Small*, 2020, **16**, 2002888.
17. S. Kumari, B. P. Ajayi, B. Kumar, J. B. Jasinski, M. K. Sunkara and J. M. Spurgeon, *Energy Environ. Sci.*, 2017, **10**, 2432-2440.
18. H. N. Nong, H. S. Oh, T. Reier, E. Willinger, M. G. Willinger, V. Petkov, D. Teschner and P. Strasser, *Angew. Chem., Int. Ed.*, 2015, **54**, 2975-2979.
19. J. Lim, D. Park, S. S. Jeon, C. W. Roh, J. Choi, D. Yoon, M. Park, H. Jung and H. Lee, *Adv. Funct. Mater.*, 2018, **28**, 1704796.
20. Y. Pi, Q. Shao, P. Wang, J. Guo and X. Huang, *Adv. Funct. Mater.*, 2017, **27**, 1700886.
21. B. M. Tackett, W. Sheng, S. Kattel, S. Yao, B. Yan, K. A. Kuttiyiel, Q. Wu and J. G. Chen, *ACS Catal.*, 2018, **8**, 2615-2621.
22. J. Wu, M. Liu, K. Chatterjee, K. P. Hackenberg, J. Shen, X. Zou, Y. Yan, J. Gu, Y. Yang and J. Lou, *Adv. Mater. Interfaces*, 2016, **3**, 1500669.
23. R. Gao, Q. Dai, F. Du, D. Yan and L. Dai, *J. Am. Chem. Soc.*, 2019, **141**, 11658-

11666.
24. M. Blasco-Ahicart, J. Soriano-López, J. J. Carbó, J. M. Poblet and J.-R. Galan-Mascaros, *Nat Chem*, 2018, **10**, 24-30.
25. J. Gao, X. Huang, W. Cai, Q. Wang, C. Jia and B. Liu, *ACS Appl. Mater. Interfaces*, 2020, **12**, 25991-26001.
26. M. Tariq, W. Q. Zaman, W. Sun, Z. Zhou, Y. Wu, L.-m. Cao and J. Yang, *ACS Sustainable Chem. Eng.*, 2018, **6**, 4854-4862.
27. J. Lim, D. Park, S. S. Jeon, C. W. Roh, J. Choi, D. Yoon, M. Park, H. Jung and H. Lee, *Adv Funct Mater*, 2018, **28**, 1704796.
28. H. Ohno, S. Nohara, K. Kakinuma, M. Uchida and H. Uchida, *Catalysts*, 2019, **9**, 74.
29. E.-J. Kim, J. Shin, J. Bak, S. J. Lee, K. hyun Kim, D. Song, J. Roh, Y. Lee, H. Kim and K.-S. Lee, *Appl .Catal. B*, 2021, **280**, 119433.
30. Z.-Y. Wu, F.-Y. Chen, B. Li, S.-W. Yu, Y. Z. Finfrock, D. M. Meira, Q.-Q. Yan, P. Zhu, M.-X. Chen and T.-W. Song, *Nat. Mater.*, 2022, 1-9.
31. V. K. Puthiyapura, M. Mamlouk, S. Pasupathi, B. G. Pollet and K. Scott, *Journal of Power Sources*, 2014, **269**, 451-460.
32. H. Lv, S. Wang, J. Li, C. Shao, W. Zhou, X. Shen, M. Xue and C. Zhang, *Applied Surface Science*, 2020, **514**, 145943.
33. G. Jiang, H. Yu, Y. Li, D. Yao, J. Chi, S. Sun and Z. Shao, *ACS Appl Mater Interfaces*, 2021, **13**, 15073-15082.